Ellingham diagram: A new look at an old tool

E. Epifano, D. Monceau

Corrosion Science xxx (xxxx) 111113

Contents lists available at ScienceDirect

Corrosion Science

journal homepage: www.elsevier.com/locate/corsci

Ellingham diagram: A new look at an old tool

E. Epifano, D. Monceau

CIRIMAT Laboratory, University of Toulouse, CNRS, INPT, UPS, ENSIACET, 4 allée Emile Monso, BP-44362, 31030 Toulouse Cedex 4, France

ARTICLE INFO

Keywords:
Ellingham diagram
High-temperature oxidation
Thermodynamic computations

ABSTRACT

Ellingham diagrams are thermodynamic tools that allow comparing the relative stability among oxides. They are well established for pure metals, but they can be obtained for any multi-element system if the chemical activity of each component is known. However, chemical activities are very difficult to obtain experimentally and, because of the lack of these data, Ellingham diagrams have never been reported for complex industrial alloys. This work aims to show how nowadays advanced thermodynamic databases can be used to supply for this lack. Herein, the Ellingham diagrams of four wildly used alloys- TiAl 48–2–2, TA6V, Inconel 718 and 304 steel- have been computed. The results are discussed in respect to the oxidation behavior of these alloys and important differences in respect to the Ellingham diagram of pure metals are highlighted.

1. Introduction

Several industrial fields, such as transportation, materials and energy productions, involve high temperature processes in oxidizing environments. Oxidation resistance is hence a fundamental criterium for alloy design in these fields. The resistance is achieved through the selective oxidation of one element of the alloy, which leads to the formation of a protective, slow growing oxide scale at its surface. The best oxide candidates for this purpose are generally alumina (Al_2O_3), chromia (Cr_2O_3) and silica (SiO_2). In order to sustain a selective oxidation, the alloy composition needs to respect several criteria which, as firstly stated by Wagner [1], are related to thermodynamic and kinetic properties of the alloy and the oxide. Among these criteria, a fundamental one concerns the thermodynamic stability of the desired protective oxide. In this respect, a useful tool is the Ellingham diagram, a graph comparing the stability of oxides as a function of the temperature.

Ellingham diagrams are obtained from basic thermodynamic laws, as they represent the Gibbs free energy change ΔG associated with a reaction of the type:

$$\frac{2a}{b}Me + O_2 \rightleftarrows \frac{2}{b}Me_aO_b \tag{1}$$

Where *Me* is a metallic element, O_2 is a gas molecule of dioxygen and Me_aO_b is an oxide.

As shown by the Eq. 1, in order to compare the stability of various oxides, reactions are written for the same quantity of oxygen, namely one mole of O_2 (or equivalently for ½ mole of O_2). For a practical point of view, this allows answering the question whether one O_2 molecule (the limiting reagent) reacts preferentially with a metal rather than another one.

The Gibbs free energy change of the reaction is generally given in respect to the **standard state of the species (°G),** which is the stable form of the species at the temperature of interest. It is then:

$$\Delta G = G - {}^{\circ}G = \frac{2}{b}\bar{G}_{Me_aO_b} - (\bar{G}_{O2} + \frac{2a}{b}\bar{G}_{Me}) \tag{2}$$

where $\bar{G}$ are the partial Gibbs energy of the species with respect to the standard state. At equilibrium, $\Delta G = 0$ as reactants and products are in equilibrium with each other. The partial Gibbs energy of each species can be rewritten as $\bar{G}_i = RTln(a_i)$, with a_i being the activity, T the absolute temperature and R the molar gas constant. Eq. 2 is then:

$${}^{\circ}G = -RT\ln\frac{a_{Me_aO_b}{}^{2/b}}{a_{Me}{}^{2a/b} \bullet a_{O2}} \tag{3}$$

If the oxidation reaction involves a pure metal, *Me* and Me_aO_b are both pure species in their standard state and by definition their activities are equal to 1. For O_2, the activity is equal to the partial pressure $p(O_2)/p(O_2)^{\circ}$, where the standard $p(O_2)^{\circ} = 1$ bar. With these simplifications, the following equation is obtained:

$${}^{\circ}G = -RT\ln\left(\frac{1}{pO_2}\right) \tag{4}$$

Based on the latter equation, Ellingham diagrams [2] have been computed for pure metals and used to predict the relative stability among oxides [3,4].

However, experimental evidences on oxidation of alloys are sometimes in contradiction with these predictions. One reason for discrepancy is obviously related to the fact that Ellingham diagrams are merely thermodynamic tools and they do not consider the kinetics: difficult nu-

https://doi.org/10.1016/j.corsci.2023.111113
Received 3 November 2022; Received in revised form 14 March 2023; Accepted 15 March 2023
0010-938/

cleation and slow diffusion of the protective alloying element, or large dissolution and fast diffusion of oxygen into the alloy can impede the formation of the most stable oxide at the surface of the alloy, and can lead to internal oxidation [1]. However, in some cases, the discrepancies between prediction and observation are due to an *inexact* use of Ellingham's diagram. As herein shown, Eq. 4 is correct only for pure metals, as the activity of pure substances is equal to 1. In alloys, the activity of each component is always < 1 and therefore Eq. 3 becomes:

$$^{\circ}G = -RT \ln \frac{1}{{a_{Me}}^{2a/b} \bullet p_{O2}} \quad (5)$$

Experimental values for activities are rare and they are not available for many industrial alloys. Therefore, Eq. 5 is rarely applied, despite the fact that it is very well known that non-ideality of metallic alloys can be large and can lower the stability of the oxide at the surface of the metal [4]. However, the development of thermodynamic databases based on the CALPHAD approach has made possible and easy to obtain activity values for any alloy composition. The aim of this work is to show how to obtain Ellingham's diagrams for multi-metallic systems and to give a few examples of their usefulness. To the best of our knowledge, Ellingham diagram for specific alloys have never been reported in the literature. For this purpose, we have selected four different alloys that are wildly used in industries: the 304 stainless steel alloy, the Inconel 718 nickel-based alloy, the TA6V titanium-based alloy and the TiAl4822 alloy. As we will see, the Ellingham diagrams of these alloys present notable differences compared to that of pure metals. The oxidation behavior of these alloys will be hence discussed in comparison with these new calculations and the advantages and limitations of Ellingham diagrams will be discussed. When studying selective oxidation, it is important to know precisely what is the most stable oxide in contact with the alloy, before to apply kinetic models which will predict if the most stable can form an external scale at the alloy surface.

2. Method

All the Ellingham diagrams shown in this work have been obtained from thermodynamic calculations performed using the Thermo-Calc software [5].

For the pure metal, the Ellingham diagram was directly obtained from Eq. 2, i.e. by subtracting the free Gibbs energy of reagents to the Gibbs free energy of the products of the oxidation reaction. The Gibbs free energy of each metal and oxide involved was calculated as a function of the temperature using Thermo-Calc.

For the alloys, Ellingham diagrams were obtained from Eq. 5. In this equation, $^{\circ}G$ is known from the previous calculation, since it is a state function and its value does not change with the reaction path. The activities of the various metals in the alloy a_{Me} were obtained as a function of the temperature from Thermo-Calc calculations. For these computations, the compositions of the alloys were set as shown in the next sections and the a_{Me} were computed as a function of the temperature T for 20 °C < T < 1500 °C, including all the phases predicted as stable in the calculations (see annex). The standard reference state was set for each element of the alloy, i.e. the stable phase of the element at each computed temperature. For instance, for aluminum, the reference state is the FCC (face-centered cubic) phase from room temperature till 660.3 °C (melting point of Al) and the liquid phase above this temperature.

The following thermodynamic databases were used for the calculations: the TCFE8 database for the 304 alloy, the TCNI9 database for Inconel 718 and the TCTI4 database for TA6V and TiAl4822.

3. Results

3.1. Ellingham's diagram for Me-O systems

Eleven different metals and their oxides were included in this work: Ni, Fe, Mo, Nb, Cr, Mn, Si, V, Ti, Al and Hf. The corresponding binary Me-O phase diagrams were computed for all the elements and they are reported in the annex.

Some elements, as for instance aluminum, present rather simple phase diagrams, where only one oxide phase is stable. For example, in the Al-O system, only the α-Al_2O_3 with corundum structure is stable, despite the existence of several polymorphic forms, that are often observed during the first stages of oxidation, being almost as stable as the main α phase [6]. Other metals, for example titanium, present complex phase diagrams, with several stable oxide phases, as shown in Fig. 1-(a).

In the case of titanium, one could wonder which oxides should be reported on the Ellingham diagram. Oxidation studies on pure titanium and titanium-based alloys for temperature T < 1000 °C consistently show the formation of a thick rutile TiO_2 scale [7,8] and sometimes the transient anatase TiO_2 on top of the scale. Rutile TiO_2 is the most stable titanium oxide under usual oxidizing atmospheres (oxygen, air etc.) and one could be interested to compare the stability of this phase with other metallic oxides. Nevertheless, Ellingham diagrams are thermodynamic tools and, according to thermodynamics, TiO_2 cannot be in equilibrium with metallic titanium. Indeed, as shown in Fig. 2, the metallic α-Ti phase can only be in equilibrium with Ti_3O_2, for T < 1193 K, and

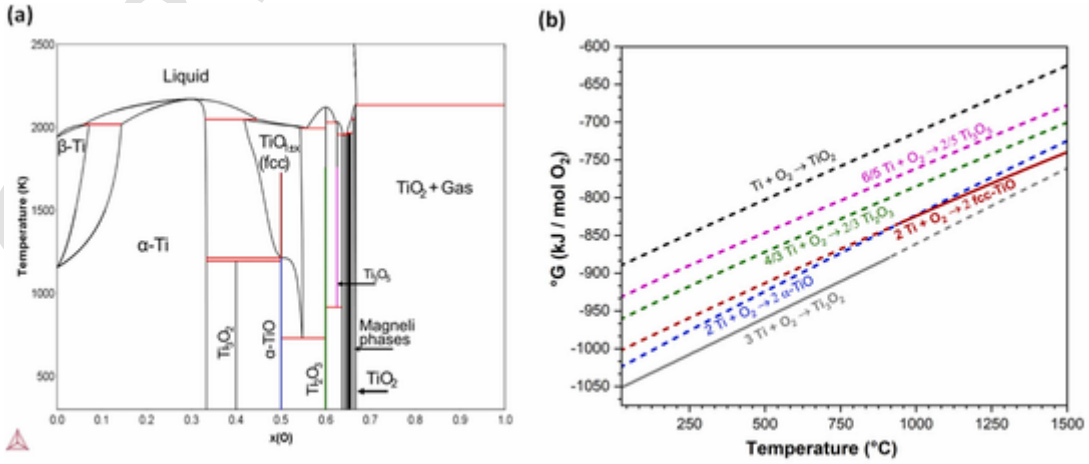

Fig. 1. (a) Ti-O phase diagram computed using the TCTI1 database from Thermo-Calc. (b) Ellingham diagram comparing the stability of various titanium oxides. Solid lines: reactions corresponding to thermodynamic equilibrium; Dashed lines: out of equilibrium reactions.

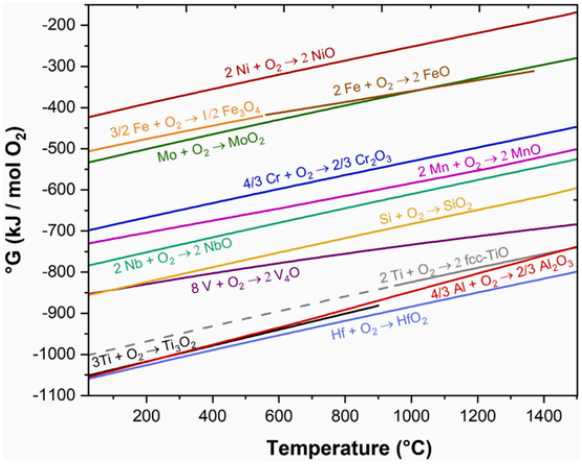

Fig. 2. Ellingham diagram for several metal/oxide reactions. Dashed lines represent the oxidation reaction of metastable oxides.

with fcc-$TiO_{1\pm x}$ above this temperature. For this reason, the correct reactions to consider for titanium are:

$$3Ti + O_2 \rightleftarrows Ti_3O_2, \text{for} T<1193K$$

$$2Ti + O_2 \rightleftarrows 2fcc - TiO, \text{for} T>1193K$$

which are reported as solid lines, in Fig. 2-(b). All the other reactions, involving Ti and oxides with a higher oxygen molar fraction, are out-of-equilibrium reactions. These are reported as dashed lines in Fig. 2-(b), with the exception of the Magneli phases, that were excluded for sake of simplicity. As expected, these reactions show higher Gibbs free energy values than the oxidation reaction leading to Ti_3O_2 and fcc-TiO. The oxides richer in oxygen are not directly formed from metallic titanium, but by subsequent reactions involving another oxide and O_2(gas). For example, according to the computed phase diagram (ignoring the Magneli phases), for T < 732 K, the sequence of reactions is:

$$3Ti + O_2 \rightleftarrows Ti_3O_2$$

$$2Ti_3O_2 + O_2 \rightleftarrows 6\alpha - TiO$$

$$4\alpha - TiO + O_2 \rightleftarrows 2Ti_2O_3$$

$$2Ti_2O_3 + O_2 \rightleftarrows 4TiO_2.$$

Similarly, at higher temperature, fcc-$TiO_{1\pm x}$ and Ti_3O_5 are involved, depending on the temperature range.

One could wonder why these oxides are not systematically observed between the rutile TiO_2 and the metallic titanium in oxidation studies. The reason is likely related to the kinetics of formation/dissolution of these phases and the diffusion of oxygen in the metallic phase, where the solubility of oxygen is very high (33 at%). A recent nano-scale characterization by transmission electron microscopy (TEM) and atom probe tomography (APT) of a Ti62426 alloy oxidized at 650 °C supports this hypothesis: α-TiO and Ti_3O_2 were observed between the rutile scale and the metallic matrix, but only over lengths of the order of tens nanometers [9].

In summary, for complex Me-O systems with several oxide phases, an Ellingham diagram should report the oxidation reaction involving the oxide with the lowest oxygen fraction, the one that can be in equilibrium with the metal. According to this, the Ellingham diagram of Fig. 2 has been computed. The result is consistent with previously reported Elligham diagrams [10].

Among the considered metals, hafnium forms the most stable oxide: the hafnia (HfO_2). For example, at 1200 °C, the Gibbs free energy change associated with the formation of HfO_2 is equal to − 850 kJ/mol, which corresponds to an extremely low oxygen partial pressure of $7 \cdot 10^{-35}$ atm. Therefore, for $p(O_2) < 7 \cdot 10^{-35}$ atm, metallic hafnium is stable, while for $p(O_2) > 7 \cdot 10^{-35}$ atm it oxidizes to form hafnia.

Above the Hf/HfO_2 reaction, there are titanium oxides and alumina (Al_2O_3), with very close values. Vanadium oxide follows. It is worth mentioning that the V-O binary system is rather complex (see annex), similarly to the Ti-O one. The oxides observed for vanadium oxidation in common environmental conditions are V_2O_5 (that is liquid above 690 °C) and VO_2 [11], but the oxide with the lowest oxygen fraction is V_4O, that is located quite low in the Ellingham diagram. Silica follows and so on. The less stable oxide reported in Fig. 2 is the halite phase NiO. At 1200 °C, the Gibbs free energy change associated with the formation of NiO is equal to − 219 kJ/mol, which corresponds to an oxygen partial pressure of 10^{-13} atm, almost 22 orders of magnitude higher than the value found for HfO_2.

3.2. Ellingham for industrial alloys

In order to compute the Ellingham diagram for a specific alloy, Eq. 5 can be rewritten as:

$$RT \ln pO_2 = {}^{\circ}G - RT \ln (a_{Me})^{2a/b} \quad (6)$$

to emphasize that pO_2 is the unknown quantity to find. Indeed, $^{\circ}G$ is equal to the reaction for the pure metal, being a state function, and the activities are obtained from the thermodynamic calculations. It is interesting to remark that the new term $RT\ ln(pO_2)$ is necessarily higher than $^{\circ}G$, since all the activities are lower than one and the logarithm is hence a negative term. Therefore, for all the reactions, the curves computed for the metal in the alloys are systematically higher than those of the pure metals, as it is shown in the following. From a practical point of view, this means that the $p(O_2)$ of equilibrium between metal/oxide are always higher for the alloys than for the pure metals. In the following, we give a few examples of Ellingham diagrams computed for common commercial structural alloys of different types.

3.2.1. Ti-48Al-2Nb-2Cr (48–2-2 or GE-48) alloy

Ti-Al alloys are a class of materials based mainly on the intermetallic γ-TiAl phase. They are generally slightly alloyed with elements such as Nb, Cr, Mo, Ta or W in order to improve the oxidation resistance and/or their mechanical properties [12]–[14]. The Ti-48Al-2 Nb-2Cr (48–2–2 or GE-48), whose nominal composition is reported in Table 1, is one of the most used Ti-Al alloys [15]. The GEnx™ and LEAP engines used TiAl (alloy 48–2–2) for their low pressure turbine blades [15].

The nominal composition of 48–2–2 alloy has been used as input for the thermodynamic computations. The stable phases as a function of temperature are reported in Fig. 3-(a) and the corresponding elemental activities are shown in Fig. 3-(b). According to the computations, the predominant phase (≈ 90 mol.%) of the alloy, from room temperature up to 1400 K is γ-TiAl, as expected. From the binary Ti-Al phase diagram, one could expect a low content of the α_2-Ti_3Al phase in equilibrium with γ-TiAl but, for T < 1200 K, an ordered BCC (body centered cubic) phase is predicted, with a maximum quantity of 11 mol.% and decreasing with the temperature. This phase, related to the high-temperature β-phase of titanium, is stabilized by the presence of Nb and Cr in the alloy, according to the calculations. However, it must be noticed that experiments generally show the presence of the α_2-Ti_3Al phase in equilibrium with γ-TiAl. This discrepancy between calculations and experimental data for the 48–2–2 alloy has been previously reported by Cakmak et al. [16], but no explanations were provided for its origin.

The application of the Ti-Al alloys is generally limited at 800 °C and most experimental data on their oxidation behavior do no exceed 900 °C. The Ellingham diagram for the 48–2–2 alloy has been computed in this temperature range and it is shown in Fig. 4, in the form of solid

Table 1
Nominal composition of the TiAl4822 alloy.

	Ti	Al	Nb	Cr
Composition (at%)	Balance	48	2	2

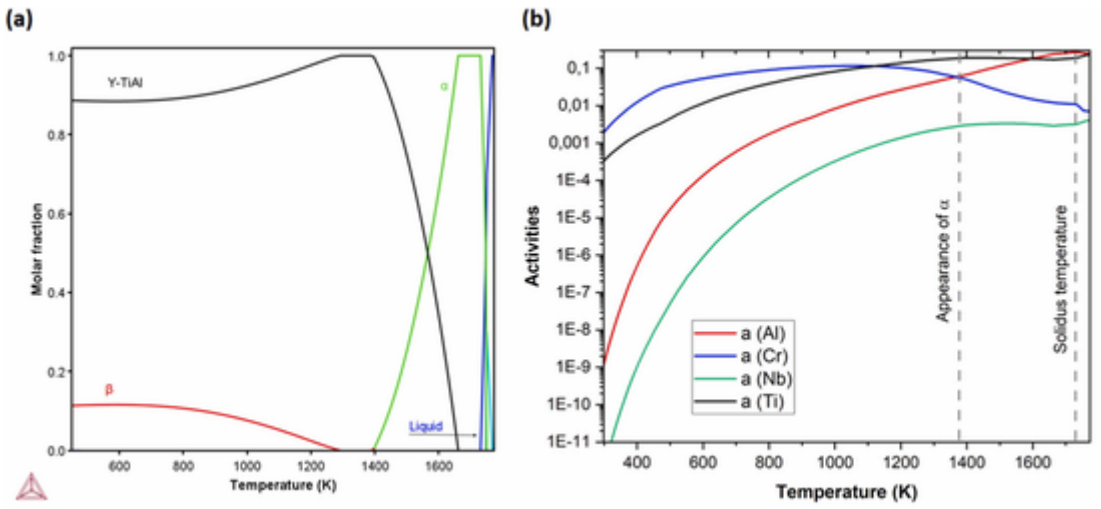

Fig. 3. (a) Phase fractions at equilibrium for the 48–2–2 alloy as a function of the temperature. (b) Ti, Al, Cr and Nb activities in 48–2–2. (Thermodynamic calculations performed using the TCTI4 database from Thermo-Calc).

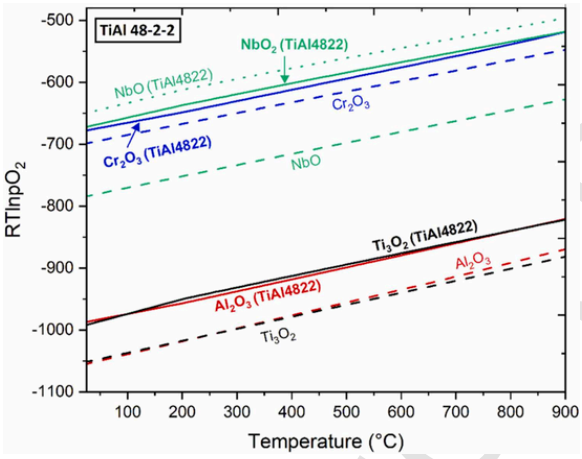

Fig. 4. Ellingham diagram for the TiAl 48–2–2 alloy (solid lines) compared to oxides in equilibrium with the pure metals (dashed lines).

lines, while the values obtained for the pure metal oxides are reported as dashed lines for comparison.

One can notice that all the curves computed for the alloy have higher pO_2 values than those obtained for the pure metals, as expected according to Eq. 6. As for the pure metals, α-Al_2O_3 and Ti_3O_2 are still the two most stable oxides among those that can be formed, with almost identical oxygen partial pressures. Several experimental evidences have reported the formation of both α-Al_2O_3 and rutile TiO_2 on the reactive surfaces of Ti-Al alloys [14], as shown in Fig. 5. Since TiO_2 is less stable than α-Al_2O_3 on pure metals, previous works [14] have generally imputed the presence of rutile only to kinetic phenomena. However, as previously explained in Section 3.1, a thorough thermodynamic analysis has to take into account all the possible titanium oxides: the formation of Ti_3O_2 competes with that of Al_2O_3 and, once Ti_3O_2 is formed, it can subsequently lead to TiO_2 by further oxidation. The massive formation of rutile generally observed on Ti-Al alloys is hence also in agreement with thermodynamics, as shown by the 48–2–2 Ellingham diagram.

Concerning the other oxides, Fig. 4 shows an inversion in the relative stability between Cr_2O_3 and niobium oxides in the alloy with respect to the pure metals: Cr_2O_3 is now more stable than niobium oxides. It is also very interesting and surprising to note that an inversion is also observed between the niobium monoxide and dioxide. According to the Nb-O phase diagram (see annex), NbO is the oxide with the lowest energy of reaction or, equivalently, the lowest partial oxygen pressures (for any temperature of practical interest, from 25 °C till thousands of °C). Therefore, as discussed in 3.1, from a thermodynamic point of view, metallic niobium cannot directly reacts to form NbO_2, the NbO

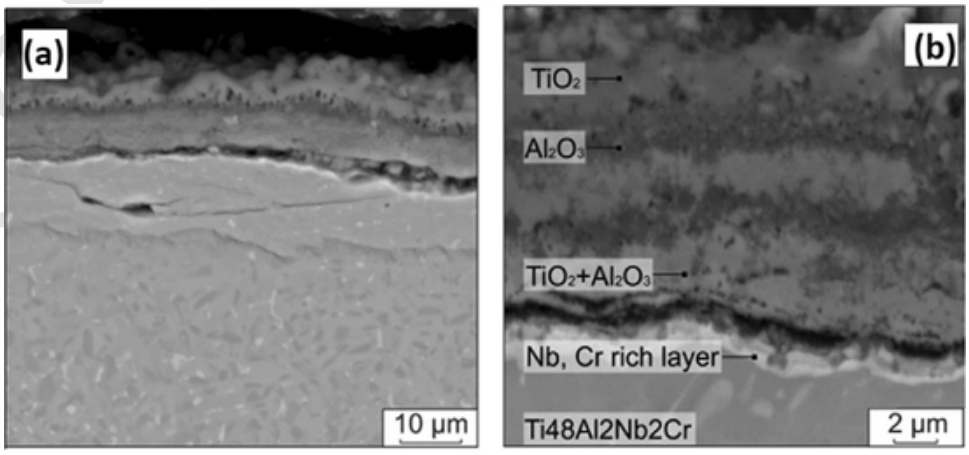

Fig. 5. TiAl 48–2–2 oxide layer after 100 h at 900 °C based on [17].

oxide must be formed in the reaction process. On the contrary, the Ellingham diagram of 48–2–2 alloy indicates that, for the alloy, NbO_2 is more stable than NbO. Mathematically, this inversion is due to the *2a/b* exponent of the metal activity in Eq. 6. More intuitively, for the oxidation of pure metals, Ellingham diagram are computed considering the oxygen as the limiting reagent, while metals are available in infinite quantities (Eq. 1). For an alloy, this is not true anymore: the metallic species present in low quantities have very low activities and this can lead to stabilize oxides with lower metallic molar fraction, as for the case of NbO_2 over NbO. This phenomenon can play a key role in the oxidation of alloy but, to the best of our knowledge, nobody has ever highlighted it before from theoretical considerations nor clearly observed it experimentally.

3.2.2. Ti-6Al-4V

The Ti-6Al-4 V alloy, generally named TA6V, is the most used titanium alloy. Its applications are limited to temperatures lower than 400 °C [18] because of creep resistance and oxygen embrittlement. Most of the experimental studies on its oxidation behavior do not exceed 700 °C [19,20].

The nominal composition (6 wt% Al, 4 wt% V, Ti balance) has been used to perform the thermodynamic computations using the TCTI3 database from Thermo-Calc (phase fractions and activities are reported in the annex). The Ellingham diagram has been drawn for the temperature range of interest, i.e. up to 700 °C, and it is reported in Fig. 6.

The oxidation reaction energies have been computed for all the binary oxides (see Ti-O and V-O phase diagrams in annex), but only the lowest values, corresponding to the most stable oxides, are reported, for sake of simplicity. From the lowest to the highest $RT\ln(pO_2)$ values, Ti_3O_2, α-Al_2O_3 and VO_4 can be observed. Therefore, contrary to the previous Ti-Al intermetallic alloy, Fig. 6 shows that the formation of titanium oxides is clearly favored in respect to alumina for the TA6V alloy. Indeed, the low concentration of aluminum implies a low Al activity, which causes a considerable increase of the pO_2 of equilibrium between the alumina and the alloy in comparison to the pure metal. On the contrary, the shift observed for the Ti_3O_2 oxide is minimum.

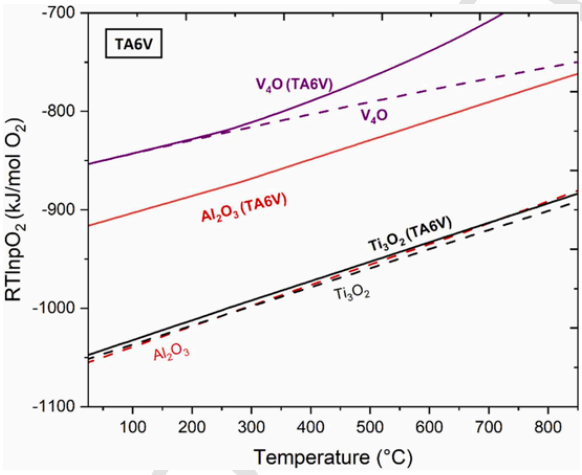

Fig. 6. Ellingham diagram for the TA6V alloy (solid lines) compared to the oxides in equilibrium with the pure metals (dashed lines).

From the Ellingham diagram, one can expect the formation of Ti_3O_2, eventually followed by other rapid oxidation reactions leading to anatase and rutile TiO_2. However, experimental studies have shown a more complex oxidation behavior for the TA6V alloy [21,22]. Indeed, oxidized TA6V alloys exhibit complex scales formed by an alternance of rutile TiO_2 and Al_2O_3 layers, with the first being always at the oxide/substrate interface and the second at the oxide/gas interface [21,22]. The micrography of a TA6V alloy oxidized under air, at 600 °C, for 500 h is shown in Fig. 7 [23]. The delamination of the oxide scale occurs certainly for the same reason than for pure titanium oxidation. It is generally attributed to the formation of pores and to the stress build-up in the oxide scale due to the large Pilling and Bedworth ratio of Ti [24]. The special arrangement of alumina and rutile layers can be attributed to diffusion. In the early stage of oxidation, a TiO_2 layer is formed, in agreement with thermodynamics. This oxide scale grows mainly due to inward diffusion of oxygen anions. Nevertheless, both aluminum and titanium cations diffuse outward through the rutile, but the first diffuses much faster than the second [25]. A kinetic demixing phenomenon [26] leading to a segregation of aluminum occurs hence at the external interface of the oxide scale, where the precipitation of Al_2O_3 occurs [22]. Once the oxide scale is detached, a new oxide scale form underneath with the same mechanism. This explanation was reported earlier for a single layer formation during the oxidation of the TiAl [27], Ti_3Al intermetallic [28] and later for TA6V for a multi-layer oxide scale [22,29].

3.2.3. Inconel 718

The Inconel 718 (IN718) is the most used nickel-based superalloy that finds applications in numerous domains (aeronautics, nuclear and other energy industries) thanks to good corrosion resistance and excellent mechanical properties. These latter are obtained thanks to the precipitation of γ'-Ni_3(Al,Ti) and γ''-Ni_3Nb precipitates in the austenitic matrix, induced by the several alloying elements present in the IN718. The typical composition, which was also adopted for the calculations, is reported in Table 2. The good oxidation resistance of the alloy is mainly related to the high chromium content, which leads to the formation of a scale mostly composed of chromia (Cr_2O_3) [30,31].

The applications of the IN718 are generally limited to 650 °C, close to the γ' *solvus*, above which a degradation of the mechanical properties occurs [32]. However, the experimental studies of the oxidation behavior of this alloy have been pushed to higher temperatures, which can be useful for alloy fabrication and heat treatments. Therefore, the Ellingham diagram of the alloy has been computed from room temperature up to 1200 °C and it is shown in Fig. 8, where solid lines represent the results for the alloy and dashed lines represent the oxides in equilibrium with the pure metals.

From lower to higher oxygen partial pressures, the following binary oxides can be predicted for IN718: Al_2O_3, titanium oxides, Cr_2O_3, NbO_2,

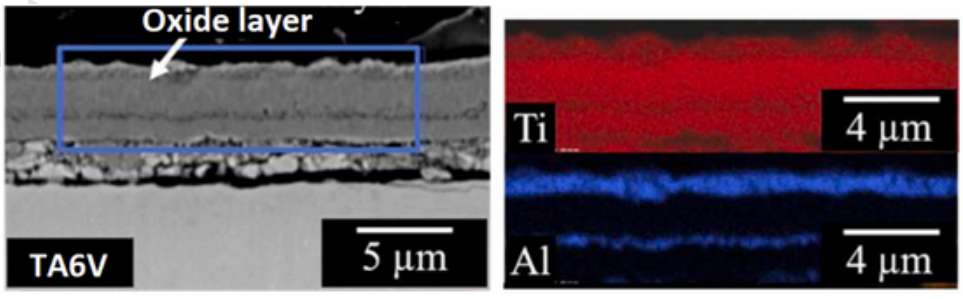

Fig. 7. A TA6V alloy after oxidation under air, at 600 °C, for 500 h [23].

Table 2
Composition of the IN718 alloy used for the thermodynamic computations.

	Ni	Fe	Cr	Nb	Mo	Si	Ti	Al
Composition (wt%)	Balance	24.6	17	4.7	2.8	0.35	0.65	0.2

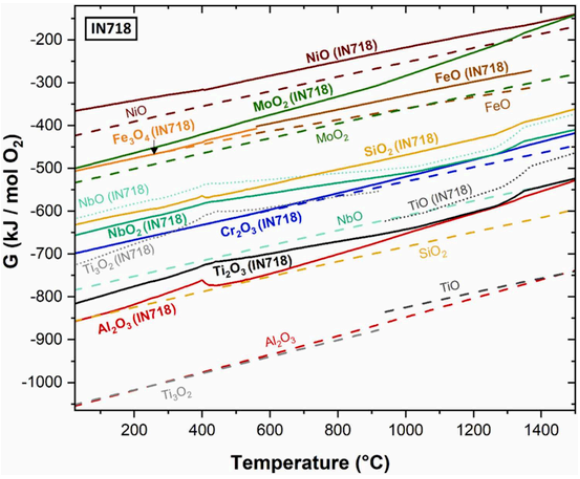

Fig. 8. Ellingham diagram for the IN718 alloy (solid and point lines) compared to the oxides in equilibrium with the pure metals (dashed lines).

SiO_2, iron oxides, MoO_2 and NiO. In complex, multi-element alloys such as IN718, ternary oxides are also likely to form. As a non-exhaustive example, the Ellingham curve of the spinel $FeCr_2O_4$ oxide was also computed and it is found between Cr_2O_3 and Fe_3O_4/FeO on the diagram.

The IN718 Ellingham diagram clearly shows the interest to perform such computations for specific alloys, since several differences can be remarked in comparison to the curves obtained for oxides in equilibrium with the pure metals. Indeed, the equilibrium of oxides formed by elements present in low concentration in the alloy are considerably shifted to higher oxygen partial pressures: it is the case for Al_2O_3, titanium oxides, SiO_2 and niobium oxides. As logical, these shifts are small for the oxides formed by elements present in high concentration, as for example Cr_2O_3, Fe oxides and NiO. In some cases, this can lead to an inversion of stability among oxides. In the IN718, this occurs for SiO_2 and NbO, that are less stable than chromia. Similarly, MoO_2 is in equilibrium with the alloy at higher oxygen pressures than iron oxides, contrary to the corresponding pure metals. Finally, similarly to the case of the TiAl 48–2–2 alloy, some inversions can be remarked in the stabilities of oxides from the same binary systems. The most stable niobium oxide for the IN718 alloy is NbO_2 and not NbO, while the titanium oxide found at lowest pO_2 is Ti_2O_3 instead of Ti_3O_5/TiO.

The Ellingham diagram computed for the IN718 alloy is consistent with several experimental evidences of the oxidation behavior of this alloy, as for instance a recent work which focused on intergranular oxidation at 850 °C [33,34]. An electron microscopy image and its relative EDS cartography from [34] are shown in Fig. 9. Below a scale mainly formed by Cr_2O_3, this study showed the presence of Al_2O_3, deep in the grain boundaries, and titanium oxides, still in the grain boundaries, but less deep than alumina [33]. Therefore, the order of observation of these oxides, from the substrate to the scale (or equivalently from the lowest to the highest oxygen partial pressures), respects their order on the Ellingham diagram. In addition, the same study reported the presence of small particles within the chromia scale, whose measured composition was $Ti_{0.43}Nb_{0.57}O_2$. The presence of a Nb-rich dioxide in contact with Cr_2O_3 is also consistent with the Ellingham diagram, where the oxide observed above Cr_2O_3 at 850 °C is NbO_2.

3.2.4. 304 alloy

The 304 stainless steel alloy is a widely used chromia forming alloy applied in several domains, including construction, oil, household appliance, food, chemical and nuclear industries. The nominal composition used for the calculations is reported in Table 3, where for simplicity the carbon content has been excluded.

The 304 alloy is generally used at room temperature or in operating conditions comprised between 300 and 850 °C. Nevertheless, oxidation studies have been conducted at higher temperature, up to 1000 °C [35] and hence the Ellingham diagram has been computed for a wider temperature range, as shown in Fig. 10.

According to the Ellingham diagram of the 304 alloy, from lower to higher oxygen partial pressures, SiO_2, Cr_2O_3, MnO, iron oxides and NiO can be expected. Some big shifts toward higher oxygen partial pressures can be observed for SiO_2 and MnO, as expected considering the low concentrations of these elements and hence their activities in the alloy. For MnO, the shift brings to an inversion of stability with Cr_2O_3, while the computed values for SiO_2 are really close to Cr_2O_3.

The Ellingham diagram well agrees with the experimental evidences [35,36]: SiO_2 is generally observed as an intergranular oxide or as a discontinuous, thin layer between the metal substrate and a Cr_2O_3 scale. In addition, some manganese-rich oxides are also observed within or on top of the Cr_2O_3 scale [35,36]. These features can be observed in the micrograph from [37] reported in Fig. 11.

The non-formation of a continuous SiO_2 scale can be easily understood by computing a second SiO_2 Ellingham curve for a 304 alloy with a slightly lower concentration, as the one shown in Fig. 12. Here, the values computed for a 0.2 wt% concentration of Si have been added (SiO_2 LC) to the Ellingham diagram of the nominal 304 composition. This new curve is above the chromia one for temperatures above 460 °C. Therefore, the concentration (or equivalently the activity) of silicon plays an important role in the 304 alloy, since it determines the relative stability between SiO_2 and Cr_2O_3.

The inversions for SiO_2 and MnO may have important consequences for the resistance to high temperature oxidation of steel 304 and of similar chromia-forming alloys. Indeed, if SiO_2 is more stable than chromia, it may form a continuous layer at the chromia/alloy interface [38]–[42]. Such a scale can act as a diffusion barrier and improve the high temperature oxidation resistance [43]. Nevertheless, it can also decrease the oxide/scale adherence [44]. Moreover, if silica and MnO are more stable than chromia, internal and intergranular oxidation of Si and Mn can occur. If MnO is less stable than chromia, it can form an external scale on top of chromia, and react with chromia to form the spinel $MnCr_2O_4$ [38,45]–[48] which is known to protect chromia from volatilization in H_2O-rich atmospheres [46,47]. However, if the manganese content is too high and MnO is more stable than Cr_2O_3, the spinel $MnCr_2O_4$ can form at the oxide/metal interface. This can decrease the oxide/scale adherence and indeed spallation has been observed in chromia-forming alloys containing more than 2% of Mn [49,50].

The high sensibility of oxidation resistance to the impurity levels is therefore highlighted by this study.

4. Discussion

Ellingham diagrams are useful tools to evaluate the relative thermodynamic stability among oxides and to provide first indications on the oxidation behavior of metals and alloys. This work shows that modern thermodynamic computations can help improving the potentiality of Ellingham diagrams and avoid some misuses or misinterpretations. More specifically, it is possible to compute Ellingham diagrams for complex multi-element and multi-phase metallic systems, considering the activities of all the present elements. This has been done herein for four different alloys, each of them representative of an important class of materials (Ti-Al, Ti-based, Ni-based alloys and stainless steels). The re-

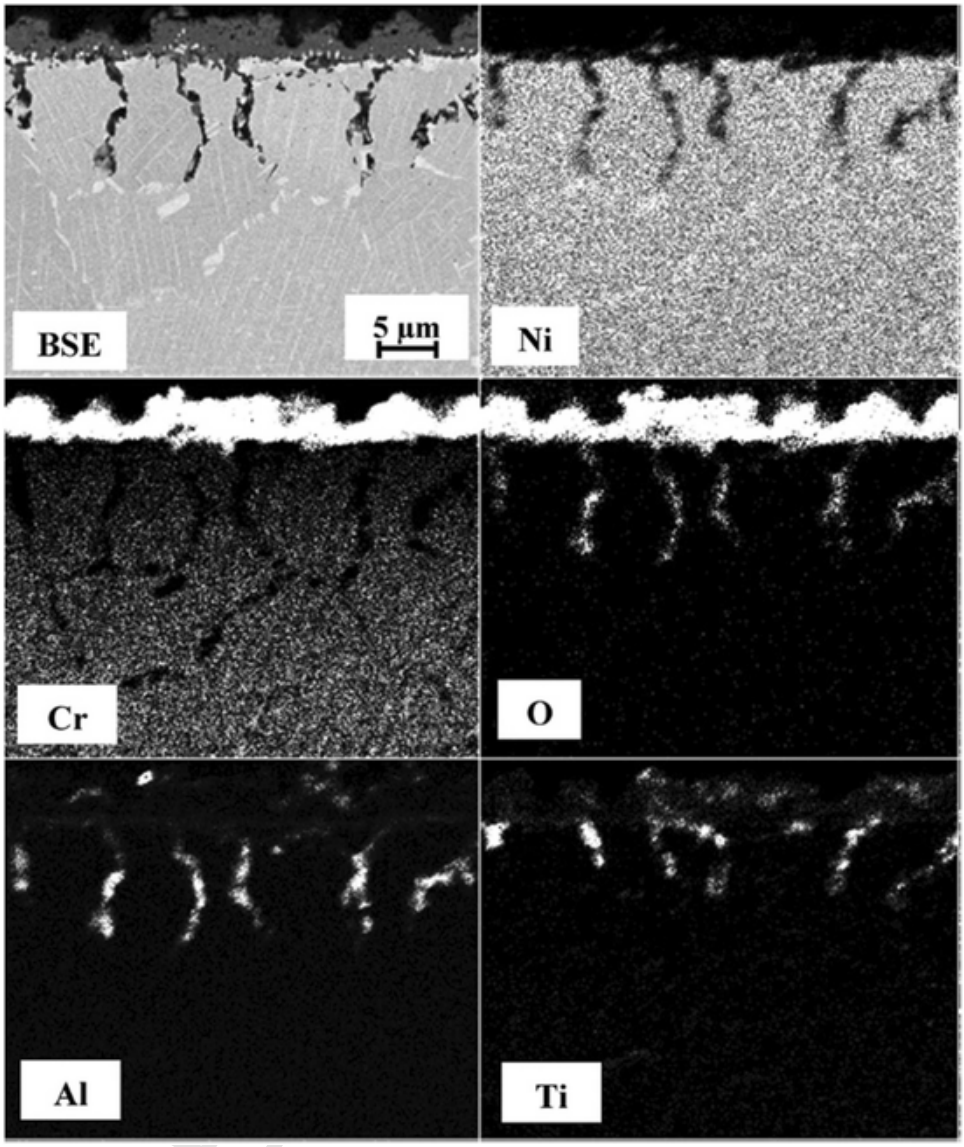

Fig. 9. EDS cartography analysis of an IN718 sample oxidized for 1000 h at 850 °C in air [34].

Table 3
Composition of the 304-alloy used in this work for the calculations.

	Fe	Cr	Ni	Mn	Si
Composition (wt%)	Balance	18.0	8.0	2.0	0.75

sults showed that, in several cases, an inversion in the relative stability of oxides can occur in alloys in comparison to the oxides in equilibrium with the pure metals. For example, SiO_2 is generally considered an oxide more stable than Cr_2O_3, on the basis of the "classical" Ellingham diagram, but this is not true for the IN718 and the 304 alloys, which are rich in chromium and poor in silicon. These more accurate Ellingham diagrams can hence help understanding and predicting the oxidation behavior of complex alloys and also the design of new ones.

Another interesting point emerged from these thermodynamic computations is the possibility to have an inversion of the relative stabilities among binary oxides belonging to the same Me-O system within an alloy. For example, the computations for IN718 shows that higher oxygen partial pressures are necessary to form NbO rather than the NbO_2, while it is clearly the opposite for metallic niobium. To the best of our knowledge, even if directly derivable from Eq. 5, this point has never been highlighted before but it could be especially useful for interpretation of

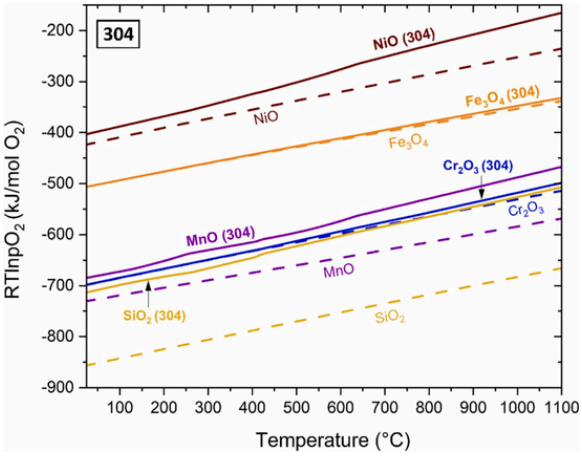

Fig. 10. Ellingham diagram for the 304 stainless steel (solid lines) compared to the oxides formed on the pure metals (dashed lines).

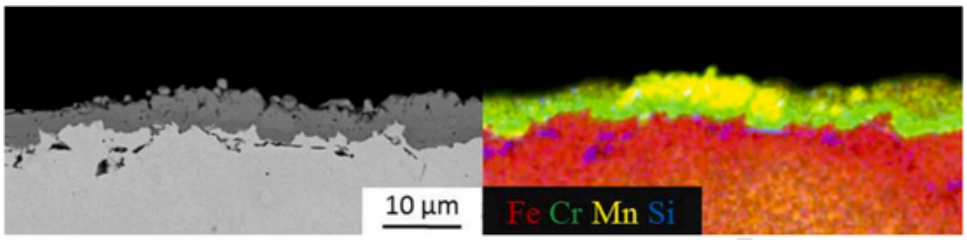

Fig. 11. 304 steel oxidized for 110 h at 850 °C under O2. Extracted from [37].

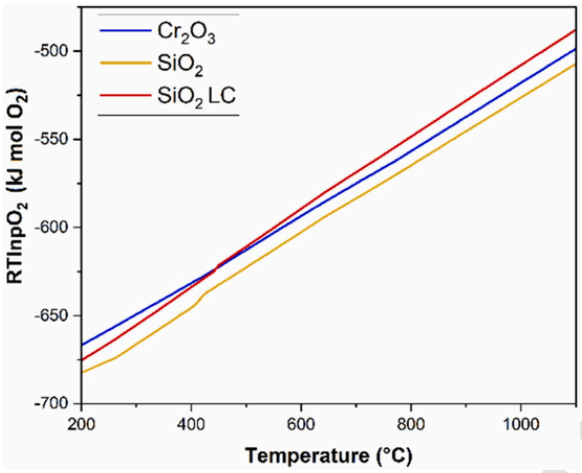

Fig. 12. Relative stability of Cr2O3 and SiO2 oxides for 304 alloy. LC = low concentration of Si, equal to 0.2 wt% instead of 0.75 wt%.

intergranular oxidation phenomena, where low oxygen partial pressures could induce these inversions.

Despite the usefulness of Ellingham diagrams for alloys, some important limitations still exist and need to be considered if one wants to use these diagrams to predict the composition of the oxide scale. First of all, from the thermodynamic point of view, there are still approximations and limitations: the solubility of the elements in all the oxides phases is not taken into account and an a priori knowledge is necessary if one wants to include ternary oxides in the calculations. Some alternative thermodynamic calculations can be performed in order to overcome these limitations, as previously shown in the literature [33]. For example, Fig. 13 reports the result of a thermodynamic computation for

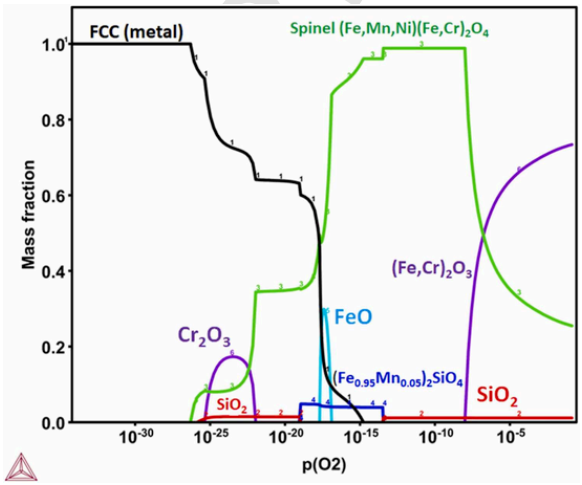

Fig. 13. Variation of the phase fraction for the 304 stainless steel composition, with increasing pO_2, at 850 °C.

a 304 steel, at 850 °C, showing the oxides forming at increasing pO_2 values. By comparing it with the Ellingham diagram of Fig. 10, one can notice that the same order of appearance is predicted for the binary oxides (SiO_2, Cr_2O_3, Mn and Fe oxides). However, Fig. 13 describes a more complex behavior, with the appearance of several ternary or multi-element oxides: a spinel phase containing Fe, Ni, Mn and Cr, a Fe-Mn silicate and a corundum phase dissolving both Cr and Fe. It is clear that these calculations give more information in comparison to an Ellingham diagram. However, these case-by-case computations require more time, knowledge and continuous access to thermodynamic databases, while Ellingham diagrams provide more immediate information.

The second fundamental limit of Ellingham diagrams (or any other thermodynamic calculations) is the lack of any kinetic knowledge which also plays a key role in oxidation and hence needs to be considered for a thorough analysis. It is well known that the thermodynamic condition, i.e. the protective oxide has to be the most stable one, is necessary but not sufficient to form the protective oxide scale [1] The kinetics aspects of the transition between internal and external oxidation have to be considered. This implies the calculation of the outward flux of the protective alloying element and of the inward flux of oxygen in the alloy [51]. Another related aspect needs to be considered. When an external chromia or alumina scale is formed, this leads often to a depletion of the alloying element below the oxide scale. Therefore, the composition of the alloy in contact with the oxide is different from the bulk composition. If the composition below the oxide scale is known, it is possible to perform a new thermodynamic calculation with this subscale alloy composition, as done in [33]. For a specific alloy, an Ellingham diagram could also be computed including impurities (O, C) that can slightly change the phase equilibria or for a range of composition, instead of simply the nominal one, in order to have some insight on the evolution of the oxidation behavior. This could be done varying the protective element content (i.e. decreasing Cr and Al content in resp. chromia- and alumina- forming alloys). It could be done also with minor elements, whose contents may vary a lot (Si, Mn, Ti, Al in chromia-forming FeNiCr alloys for example) leading to large variations of their equilibrium oxygen partial pressures.

5. Conclusions

Ellingham diagrams are useful thermodynamic tools that have been used for the decades to evaluate the relative stability among oxides. This work aims to show how nowadays advanced thermodynamic databases can be used in order to compute Ellingham diagrams for multi-element alloys. As herein shown, these often exhibit remarkable differences in comparison to the Ellingham diagram for pure metals, since the activities of the various elements in a complex alloy can be very far from unity. Chemical activities are very difficult to obtain experimentally and the lack of these data explains why Ellingham diagrams were not previously computed for individual alloys. Nowadays, the development of thermodynamic databases allows calculating the chemical activities and hence Ellingham diagrams for specific alloys in a much easier way. This has been shown in this work for four common alloys: TiAl 48–2–2, TA6V, 304 and IN718. Several inversions in the relative stability among oxides in comparison to the "classical" Ellingham diagrams

have been highlighted, some of which can shade lights on the oxidation behavior of these alloys.

Uncited reference

[13,39–41].

Declaration of Competing Interest

The authors declare that they have no known competing financial interests or personal relationships that could have appeared to influence the work reported in this paper.

Data availability

No data was used for the research described in the article.

Appendix A. Supporting information

Supplementary data associated with this article can be found in the online version at doi:10.1016/j.corsci.2023.111113.

References

[1] C. Wagner, Theoretical analysis of the diffusion processes determining the oxidation rate of alloys, J. Electrochem. Soc. 99 (1952) 369, https://doi.org/10.1149/1.2779605.

[2] E.H.J. T, Reducibility of oxides and sulphides in metallurgical processes, J. Soc. Chem. Ind. London, 63, n° 5, 125.

[3] S.R.J. Saunders, J.R. Nicholls, Chapter 14 - Oxidation, hot corrosion and protection of metallic materials, in Physical Metallurgy (Fourth Edition), R.W. Cahn et P. Haasen, Éd. Oxford: North-Holland, 1996, pp. 1291–1361. doi: 10.1016/B978–044489875-3/50019–3.).

[4] Young David John, High temperature oxidation and corrosion of metals, vol. 1, 2008.

[5] J.-O. Andersson, T. Helander, L. Höglund, P. Shi, B. Sundman, Thermo-Calc & DICTRA, computational tools for materials science, Calphad 26 (2) (2002) 273–312, https://doi.org/10.1016/S0364-5916(02)00037-8.

[6] H.A. Wriedt, The Al-O (Aluminum-Oxygen) system, Bull. Alloy Phase Diagr. 6 (6) (1985) 548–553, https://doi.org/10.1007/BF02887157.

[7] G.R. Wallwork, A.E. Jenkins, Oxidation of titanium, zirconium, and hafnium, J. Electrochem. Soc. 106 (1) (1959) 10, https://doi.org/10.1149/1.2427248.

[8] D. Siva Rama Krishna, Y.L. Brama, Y. Sun, Thick rutile layer on titanium for tribological applications, Tribol. Int. 40 (2) (2007) 329–334, https://doi.org/10.1016/j.triboint.2005.08.004.

[9] C. Dupressoire, et al., The role of nitrogen in the oxidation behaviour of a Ti6242S alloy: a nanoscale investigation by atom probe tomography, Acta Mater. 216 (2021) 117134, https://doi.org/10.1016/j.actamat.2021.117134.

[10] ASM International, ASM Handbook, 10th ed, ASM International, Materials Park, Ohio, 1990.

[11] J.G. Keller, D.L. Douglass, The high-temperature oxidation behavior of vanadium-aluminum alloys, Oxid. Met 36 (5) (1991) 439–464, https://doi.org/10.1007/BF01151591.

[12] M. Schmitz-Niederau, M. Schutze, The oxidation behavior of several Ti-Al alloys at 900°C in air, Oxid. Met. 52 (3) (1999) 225–240, https://doi.org/10.1023/A:1018839511102.

[13] J. Małecka, Transformation and precipitation processes in a metal substrate of oxidized tial-based alloys, Oxid. Met 91 (3) (2019) 365–380, https://doi.org/10.1007/s11085-019-09886-1.

[14] W. Zhu, Y. He, X. Cui, Y. He, B. Li, C. Zhang, Microstructure refinement and oxidation behavior improvement in Mo modified TiAl4822 alloy prepared by vacuum sintering, Vacuum 202 (2022) 111122, https://doi.org/10.1016/j.vacuum.2022.111122.

[15] B. Duan, et al., History and development of γ-TiAl alloys and the effect of alloying elements on their phase transformations, J. Alloy. Compd. 909 (2022) 164811, https://doi.org/10.1016/j.jallcom.2022.164811.

[16] E. Cakmak, et al., A comprehensive study on the fabrication and characterization of Ti–48Al–2Cr–2Nb preforms manufactured using electron beam melting, Materialia 6 (2019) 100284, https://doi.org/10.1016/j.mtla.2019.100284.

[17] Iu.N. Maliutina, H. Si-Mohand, J. Sijobert, Ph Bertrand, D.V. Lazurenko, I.A. Bataev, Structure and oxidation behavior of γ-TiAl coating produced by laser cladding on titanium alloy, Surf. Coat. Technol. 319 (2017) 136–144, https://doi.org/10.1016/j.surfcoat.2017.04.008.

[18] R.R. Boyer, Titanium for aerospace: rationale and applications, Adv. Perform. Mater. 2 (4) (1995) 349–368, https://doi.org/10.1007/BF00705316.

[19] S. Frangini, A. Mignone, F. de Riccardis, Various aspects of the air oxidation behaviour of a Ti6Al4V alloy at temperatures in the range 600–700 °C, J. Mater. Sci. 29 (3) (1994) 714–720, https://doi.org/10.1007/BF00445984.

[20] N. Vaché, Y. Cadoret, B. Dod, D. Monceau, Modeling the oxidation kinetics of titanium alloys: review, method and application to Ti-64 and Ti-6242s alloys, Corros. Sci. 178 (2021) 109041, https://doi.org/10.1016/j.corsci.2020.109041.

[21] C. Coddet, P. Sarrazin, J. Besson, Essai d'interprétation du mécanisme d'oxydation de l'alliage de titane TA6V4 par l'oxygène sec entre 700°C et 1000°C, J. Less Common Met. 51 (1) (1977) 1–12, https://doi.org/10.1016/0022-5088(77)90168-0.

[22] H.L. Du, P.K. Datta, D.B. Lewis, J.S. Burnellgray, Air oxidation behavior of Ti-6al-4v alloy between 650-Degrees-C and 850-Degrees-C, Corros. Sci. 36 (4) (1994) 631–642.

[23] A. Casadebaigt, Etude de l'oxydation à chaud d'échantillons en alliage TA6V élaborés par fabrication additive. Conséquences sur les propriétés mécaniques., Ph.D thesis, Toulouse, INPT, 2020. Available at: https://www.theses.fr/2020INPT0103.

[24] J. Stringer, The oxidation of titanium in oxygen at high temperatures, Acta Metall. 8 (1960) 758–766.

[25] J.A.S. Ikeda, Y.M. Chiang, B.D. Fabes, Nonequilibrium surface segregation in aluminium-doped TiO2 under an oxidizing potential: effects on redox color-boundary migration, J. Am. Ceram. Soc. 73 (6) (1990) 1633–1640.

[26] H. Schmalzried, et W. Laqua, Multicomponent oxides in oxygen potential gradients, Oxid. Met. 15 (3/4) (1981) 339–353.

[27] S. Becker, A. Rahmel, M. Schorr, M. Schütze, Mechanism of isothermal oxidation of the intel-metallic TiAl and of TiAl alloys, Oxid. Met 38 (5) (1992) 425–464, https://doi.org/10.1007/BF00665663.

[28] J. Rakowski, D. Monceau, F.S. Pettit, G.H. Meier, et R.A. Perkins, Microscopy of Oxidation 2: Proceedings of the Second International Conference on the Microscopy of Oxidation Held at Selwyn College, the University of Cambridge, p. 476–487, 1993.

[29] A. Casadebaigt, J. Hugues, D. Monceau, High temperature oxidation and embrittlement at 500–600 °C of Ti-6Al-4V alloy fabricated by Laser and Electron Beam Melting, Corros. Sci. 175 (2020) 108875.

[30] C.S. Giggins, F.S. Pettit, Oxidation of Ni-Cr-Al alloys between 1000° and 1200°C, J. Electrochem. Soc. 118 (11) (1971) 1782–1790.

[31] G.A. Greene, C.C. Finfrock, Oxidation of inconel 718 in air at high temperatures, Oxid. Met. 55 (5/6) (2001) 505–521.

[32] R.E. Schafrik, D.D. Ward, et J.R. Groh, Application of Alloy 718 in GE Aircraft Engines: Past, Present and Next Five Years, The Minerals, Metals & Materials Society, vol. Superalloys 718, 625, 706 and Various Derivaties, p. 1–12, 2001.

[33] T. Sanviemvongsak, D. Monceau, C. Desgranges, B. Macquaire, Intergranular oxidation of Ni-base alloy 718 with a focus on additive manufacturing, Corros. Sci. 170 (2020) 108684, https://doi.org/10.1016/j.corsci.2020.108684.

[34] T. Sanviemvongsak, D. Monceau, B. Macquaire, High temperature oxidation of IN 718 manufactured by laser beam melting and electron beam melting: effect of surface topography, Corros. Sci. 141 (2018) 127–145, https://doi.org/10.1016/j.corsci.2018.07.005.

[35] X.C. Cai, et al., Superior high-temperature oxidation resistance of nanocrystalline 304 austenitic stainless steel containing a small amount of Si, Scr. Mater. 204 (2021) 114155, https://doi.org/10.1016/j.scriptamat.2021.114155.

[36] S.G. Wang, M. Sun, H.B. Han, K. Long, Z.D. Zhang, The high-temperature oxidation of bulk nanocrystalline 304 stainless steel in air, Corros. Sci. 72 (2013) 64–72, https://doi.org/10.1016/j.corsci.2013.03.008.

[37] A. Col, Étude de l'oxydation catastrophique de l'acier 304L: mécanismes et effet d'une pré-déformation, Ph.D Thesis, Université Grenoble Alpes, 2016.

[38] T.D. Nguyen, J. Zhang, D.J. Young, Effects of silicon on high temperature corrosion of Fe-Cr and Fe-Cr-Ni alloys in carbon dioxide, Oxid. Met. 81 (5–6) (2014) 549–574.

[39] B. Li, et B. Gleeson, Effects of silicon on the oxidation behavior of ni-base chromia-forming alloys, Oxid. Met. 65 (1) (2006) 101–122.

[40] S. Mathieu, L. Aranda, L. Portebois, S. Mathieu, M. Vilasi, On the pre-oxidation treatments of four commercial Ni-based superalloys in air and in Ar–H2O at 950 °C, Oxid. Met. 90 (1–2) (2018) 43–63, https://doi.org/10.1007/s11085-017-9822-5.

[41] H. Ackermann, G. Teneva-Kosseva, K. Lucka, H. Köhne, S. Richter, J. Mayer, Oxidation behaviour of Ni–Cr based alloy containing Si during high temperature application in an oil burner, Corros. Eng. Sci. Technol. 45 (6) (2010) 468–474, https://doi.org/10.1179/174327809×397811.

[42] B. Ahmad, P. Fox, STEM analysis of the transient oxidation of a Ni-20Cr alloy at high temperature, Oxid. Met. 52 (1) (1999) 113–138, https://doi.org/10.1023/A:1018827108376.

[43] L. Mikkelsen, S. Linderoth, J.B. Bilde-Sørensen, The effect of silicon addition on the high temperature oxidation of a Fe-Cr alloy, Mater. Sci. Forum 461–464 (2004) 117–122, https://doi.org/10.4028/www.scientific.net/MSF.461-464.117.

[44] T. Perez, Oxydation à haute température d'alliages modèles Ni-25Cr, Influence des éléments mineurs Mn et Si sur les mécanismes de croissance des oxydes protecteurs, These de doctorat, Université de Lorraine, 2019. Available at: ⟨https://www.theses.fr/2019LORR0234⟩.

[45] L. Liu, S. Wu, Y. Dong, S. Lü, Effects of alloyed Mn on oxidation behaviour of a Co–Ni–Cr–Fe alloy between 1050 and 1250°C, Corros. Sci. 104 (2016) 236–247, https://doi.org/10.1016/j.corsci.2015.12.016.

[46] M. Hänsel, L. Garcia-Fresnillo, S.L. Tobing, U. Breuer, et V. Shemet, Hydrogen Uptake and Hydrogen Profiles in Chromia Scales Formed on Ni25Cr(Mn) in Low pO_2 Test Gases at 1000°C, presented at Advanced Fossil Fuel Energy Technologies, Hydrogen Production and, 2010, p. 59–64. doi: 10.4028/www.scientific.net/AST.72.59.

[47] G.R. Holcomb, D.E. Alman, The effect of manganese additions on the reactive evaporation of chromium in Ni–Cr alloys, Scr. Mater. 54 (10) (2006) 1821–1825, https://doi.org/10.1016/j.scriptamat.2006.01.026.

[48] D.L. Douglass, J.S. Armijo, The effect of silicon and manganese on the oxidation

mechanism of Ni-20 Cr, Oxid. Met. 2 (2) (1970) 207–231, https://doi.org/10.1007/BF00603657.
[49] F.H. Stott, F.I. Wei, C.A. Enahoro, The influence of manganese on the high-temperature oxidation of iron-chromium alloys, Mater. Corros. 40 (4) (1989) 198–205, https://doi.org/10.1002/maco.19890400403.
[50] J. Zurek, et al., Growth and adherence of chromia based surface scales on Ni-base alloys in high- and low-pO(2) gases, Mater. Sci. Eng. a Struct. Mater. Prop. Microstruct. Process. 477 (1–2) (2008) 259–270, https://doi.org/10.1016/j.msea.2007.05.035.
[51] R.A. Rapp, The transition from internal to external oxidation and the formation of interruption bands in silver-indium alloys, Acta Metall. 9 (8) (1961) 730–741, https://doi.org/10.1016/0001-6160(61)90103-1.